Darryl Overby

Jeffrey Ruberti[1]

MIT,
Cambridge, MA 02138

Haiyan Gong

Thomas F. Freddo

Boston University School of Medicine,
Boston, MA 02215

Mark Johnson[1]

MIT,
Cambridge, MA 02138

Specific Hydraulic Conductivity of Corneal Stroma as Seen by Quick-Freeze/Deep-Etch

Previous studies of the hydraulic conductivity of connective tissues have failed to show a correspondence between ultrastructure and specific hydraulic conductivity. We used the technique of quick-freeze/deep-etch to examine the ultrastructure of the corneal stroma and then utilized morphometric studies to compute the specific hydraulic conductivity of the corneal stroma. Our studies demonstrated ultrastructural elements of the extracellular matrix of the corneal stroma that are not seen using conventional electron microscopic techniques. Furthermore, we found that these structures may be responsible for generating the high flow resistance characteristic of connective tissues. From analysis of micrographs corrected for depth-of-field effects, we used Carmen-Kozeny theory to bound a morphometrically determined specific hydraulic conductivity of the corneal stroma between 0.46×10^{-14} *and* $10.3\times10^{-14}\,cm^2$. *These bounds encompass experimentally measured values in the literature of* 0.5×10^{-14} *to* $2\times10^{-14}\,cm^2$. *The largest source of uncertainty was due to the depth-of-field estimates that ranged from 15 to 51 nm; a better estimate would substantially reduce the uncertainty of these morphometrically determined values.* [DOI: 10.1115/1.1351888]

1 Introduction

The interstitial spaces in connective tissues are, for the most part, perfused with a flow of fluid that transports nutrients and removes waste products. These flows include the lymphatic flow that permeates the interstitium and more specialized flows such as occur in cartilage [1], intervertebral disk [2], the glomerular basement membrane [3], the arachnoid villi in the brain [4], and the aqueous outflow system in the eye [5]. Flow through these tissues is described by Darcy's law for flow through porous media, relating superficial fluid velocity, U, to the pressure gradient, ∇P,

$$U = -\frac{K}{\mu}\nabla P \tag{1}$$

where μ is the fluid viscosity and K is the specific hydraulic conductivity of the tissue [6].

While K has been experimentally measured for a wide variety of connective tissues, previous attempts to predict K based on the ultrastructure of the extracellular matrix as seen by electron microscopy have been unsuccessful [5,6]. This is likely due to collapse of glycosaminoglycans caused by conventional electron-microscopic tissue preparation methods [7], and the concomitant loss of the fine structures of the extracellular matrix or actual loss of the materials themselves.

Quick-freeze/deep-etch is a technique that has been shown to better preserve the ultrastructure of the extracellular matrix as compared to conventional techniques [8]. Briefly, the tissue is very rapidly frozen, fractured and then ''etched'' by a process in which vitrified water is sublimated away at the fractured surface leaving only frozen matrix behind. This frozen matrix is then rotary shadowed with a platinum/carbon mixture, creating a replica that is backed with more carbon for stability. The tissue is then dissolved away and the replica is viewed using a transmission electron microscope.

In the current study, we have used quick-freeze/deep-etch to examine the ultrastructure of the extracellular matrix of the bovine corneal stroma. Corneal stroma was chosen as it is a relatively homogeneous structure with known specific hydraulic conductivity [9–13]. Using electron micrographs of the quick-freeze/deep-etch replicas, we computed the specific hydraulic conductivity of this tissue using conventional porous media theories while incorporating stereological corrections for the depth-of-field of the image. The values of K computed from the micrographs were compared with experimental values available in the literature.

2 Methods

2.1 Conventional and Quick-Freeze/Deep-Etch Transmission Electron Micrographs. Fresh enucleated calf eyes were obtained from a local abattoir (Arena and Sons, Hopkinton, MA) within 1 hour of death. The enucleated eyes were opened at the equator and the lens and anterior uvea were removed. The remaining cornea and scleral rim were immersion fixed in 2 percent formaldehyde/2.5 percent glutaraldehyde in phosphate buffer (pH 7.4) for one hour. The corneas were then cut into 2×2 mm pieces and washed in phosphate buffered saline.

For conventional EM preparation, specimens were postfixed in 1 percent osmium tetraoxide and 1.5 percent potassium ferrocyanide in distilled water, and then dehydrated and embedded in an Epon-Araldite mixture. Ultrathin sections (90 nm) were cut on an ultramicrotome, counter-stained with uranyl acetate and lead citrate, and then examined with a Phillips-300 electron microscope.

For quick-freeze/deep-etch, the specimens were mounted onto 3 mm gold specimen carriers with a thin layer of 25 percent polyvinyl alcohol (Gelvatol 20–30; Monsanto, Springfield, MA) in 25 percent glycerol. The specimens were then rapidly frozen in liquid propane (−180 to −190°C) using the BAL-TEC TFD 010 plunge-freeze and transfer device (BAL-TEC limited, Principality of Liechtenstein). The frozen specimens were stored in liquid nitrogen until transferred into a cold stage (−150°C) in Balzers freeze-fracture device (BAF-301; Balzers High Vacuum, Santa Ana, CA).

Specimen holder was warmed to −100°C and fractured at the same temperature in a vacuum of 10^{-7} torr. The fractured surface was etched for 20–30 minutes by placing the cooled knife

[1]Currently at Northwestern University, Evanston, IL.

Contributed by the Bioengineering Division for publication in the JOURNAL OF BIOMECHANICAL ENGINEERING. Manuscript received by the Bioengineering Division Jan. 2000; revised manuscript received Oct. 2000. Associate Editor: C. Ross Ethier.

(−180°C) above the specimen, to expose the tissue structure. Following etching, the specimens were rotary shadowed at a 20 deg angle with platinum-carbon. The estimated electron dense coating thickness using this method was approximately 1.5–2.0 nm as determined by a quartz crystal thin film monitor. Replicas were strengthened by evaporation of carbon at an angle of 90 deg. Following shadowing, the specimen with the replica coating was stored in methanol overnight and then digested in 5 percent sodium hypochlorite containing 10–15 percent potassium hydroxide. The remaining replicas are washed several times in distilled water and floated onto copper Gilder grids (Electron Microscopy Sciences, Ft. Washington, PA). The replicas were examined and pictures taken using a Phillips-300 transmission electron microscope (Philips, Eindhoven, The Netherlands). Some stereo images (±6 deg) of the replicas were generated on a Phillips-300 transmission electron microscope outfitted with a goniometer (Philips, Eindhoven, The Netherlands).

2.2 Calculation of *K* Using Carmen-Kozeny Theory. Carmen [14] and Kozeny presented a general expression that relates the specific hydraulic conductivity of a porous medium to geometric parameters characterizing that medium, in particular, the porosity (ε: ratio of volume available for fluid flow to total tissue volume) and the specific surface area (α: ratio of wetted surface area of fluid flow channels to total tissue volume):

$$K = \frac{\varepsilon^3}{k_0 \alpha^2} \tag{2}$$

where k_0 is the Kozeny constant that depends weakly on geometry of the flow passages, and for $\varepsilon > 0.9$, depends strongly on ε [15]. For $\varepsilon < 0.8$, k_0 is not very sensitive to geometry or porosity, and is usually reported to have a value of 4–7 [5,14,16–18]. In this study, we use a value of 5 for the Kozeny constant as the porosity is always found to be less than 0.8 in the corneal stroma (note that the porosity, defined by the channel area available for fluid flow, is different than the water fraction of the tissue which is much higher: see Section 4).

Our goal was to determine ε and α from the micrographs and then use equation (2) to compute *K*. This was the approach taken by Ethier et al. [5] to characterize the hydraulic conductivity of the juxtacanalicular connective tissue in the eye. However, two considerations prevent simple application of this formula. First, the Carmen-Kozeny relationship is valid for a homogeneous matrix containing a single characteristic dimension; corneal stroma contains both collagen fibrils, with a typical diameter of 36 nm [19], and an interfibrillar matrix with a much smaller characteristic dimension. Second, the quick-freeze/deep-etch replicas are three-dimensional objects that are projected onto a two-dimensional micrograph. Stereologic theory is required to relate the projected image to the three-dimensional structure. While the former consideration is considered below, the stereologic theory is more complicated and is discussed in the next section.

The two hydrodynamic length scales in the cornea can be addressed in detail by using Debye-Brinkman theory [20]. However, when these two length scales are quite disparate, the major effects of the larger fibrils are simply to decrease the cross-sectional area available for flow, and to increase the tortuosity of the flow path. If the volume fraction of the corneal stroma is Φ_c, then the specific hydraulic conductivity of the stroma (*K*) can be related to the interfibrillar specific hydraulic conductivity (K_i) as [21,20]:

$$K = K_i \frac{1-\Phi_c}{1+\Phi_c} \tag{3}$$

As the collagen fraction of the cornea is well-known, our goal was to determine K_i of the interfibrillar regions from the quick-freeze/deep-etch micrographs. We used a value of $\Phi_c = 0.29$ based on data obtained from x-ray synchrotron analysis [19].

2.3 Determination of Porosity and Specific Surface in the Interfibrillar Region. Micrographs were scanned into TIFF format using a flatbed SilverScan II image scanner (La Cie USA, Oregon) at 400 pixels per cm. Image analysis was performed using NIH Image version 1.62 on a Macintosh G3. Prior to analysis, pixel values were inverted so that darker regions correspond open passages. As we were interested in the specific hydraulic conductivity of the interfibrillar space, regions between collagen fibrils were outlined for subsequent analysis.

To define the passages available for flow in the interfibrillar space, a threshold pixel value was selected and all pixels darker than this threshold value were considered to be available for fluid flow. The assignment of the threshold pixel value was necessarily somewhat subjective, and was complicated by contrast gradients inherent in picture development. To account for this variability, a range of threshold values was chosen visually using NIH Image to subjectively set the minimum and maximum pore sizes. An example of this thresholding is shown in Figs. 3*b* (low threshold) and 3*c* (high threshold).

After the pores had been identified using the thresholding procedure, NIH image was used to compute the total pore area per area of analysis (ε') and total perimeter per area of analysis (α'). The following adjustments were made to the perimeter result determined using NIH Image: (i) the artifactual perimeter resulting from the intersection of a pore with the boundary of the interfibrillar region was subtracted and (ii) the unaccounted internal perimeter of an annularlike pore was added.

To compute the specific hydraulic conductivity of the tissue, we required ε and α, which are parameters describing the three-dimensional tissue ultrastructure. To estimate these parameters from ε' and α', the parameters measured using the two-dimensional morphometric image, we followed the general stereologic formulation of Miles [22] and Underwood [23]. The detailed derivation of the stereological equations is given in the Appendix.

The resulting relationships are found to be

$$\varepsilon' = \varepsilon \exp\left(\frac{-\alpha D_f}{4\varepsilon}\right) \tag{4a}$$

$$\alpha' = \frac{\alpha\pi}{4} \exp\left(\frac{-\alpha D_f}{4\varepsilon}\right)\left[1 + \frac{D_f}{D_p} + \frac{\alpha D_f}{4\varepsilon}\right] \tag{4b}$$

where D_f is the depth-of-field of the projected image (the micrograph) and D_p (defined in the Appendix) is a characteristic dimension of a typical particle comprising the interfibrillar network. Note that for vanishingly small D_f, equation (4*a*) yields the Delesse principle [24] that $\varepsilon' = \varepsilon$, as assumed by Ethier et al. [5] in their analysis. The limiting behavior of equation (4*b*) shows that $\alpha' = \pi\alpha/4$ [25], which is different than that assumed by Ethier et al. (they assumed that $\alpha' = \alpha$).

To use equations (4*a*) and (4*b*) to solve for ε and α, we required two additional parameters: D_p and D_f. D_p is a weak function of particle shape and as shown in the Appendix, its value can be bounded as

$$\frac{3\pi}{2}\frac{1-\varepsilon}{\alpha} \leq D_p \leq 2\pi\frac{1-\varepsilon}{\alpha} \tag{5}$$

Equation (5) (either the lower or upper limit, as appropriate) was substituted into equation (4), allowing ε' and α' to be determined as a function of ε, α and D_f. For a particular value of ε', α' and D_f, ε and α were determined numerically.

The depth-of-field of the replicas is determined by the depth to which the platinum-carbon mixture penetrates into the exposed, etched corneal tissue. D_f would be expected to depend on (i) the angle of the evaporation gun relative to the plane of corneal tissue, and (ii) the porosity of the tissue. An increase in either of these two parameters would be expected to decrease the probability of intersection of the platinum atoms with the tissue at any horizontal plane and thus increase D_f. However, we know of no experimental studies verifying these theoretical considerations.

To measure D_f, stereo images of the replica were generated and the maximum penetration depth was estimated from the relative displacements between structures in two micrographs of a given replica taken with a +6 deg and a −6 deg rotation, respectively, using a goniometer. The vertical distance (Δy) between two structures that appeared on an image was calculated as $\Delta y = \Delta l/2 \sin\theta$ where θ=6 deg is the goniometer angle set on the microscope, l is the horizontal distance between two interfibrillar structures identified on both micrographs, and Δl is the change in that distance due to the rotation of the replica through 2θ. To minimize the chance of including vertical displacements due to large scale surface undulations, l was kept below a threshold of 100 nm. By taking several measurements in a particular interfibrillar area, a range of Δy was determined. D_f of that interfibrillar region was set to be the maximum value of Δy found in that region. The procedure was repeated in five interfibrillar regions per pair of stereo images to determine a range of values for D_f.

With a range of values for D_p and D_f determined, equations (4*a*) and (4*b*) were used to find a range of values for ε and α for a given mean value of ε' and α', and then equations (2) and (3) were applied compute a range of specific hydraulic conductivity (K) of the corneal stroma. These values were then compared with experimental measurements in the literature.

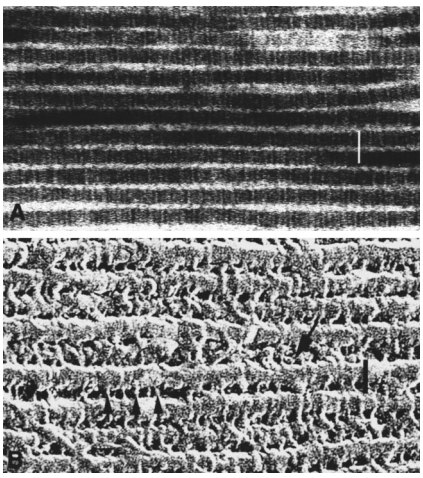

Fig. 2 (*a*) **Conventional transmission electron micrograph of bovine corneal stroma with characteristic collagen banding pattern,** (*b*) **quick-freeze/deep-etch micrograph of bovine corneal stroma. Note the enhanced resolution of the interfibrillar structures; bars: 50 nm.**

3 Results

3.1 Computation Validation of Stereologic Theory. To validate the stereological equations (4*a*) and (4*b*), predictions from the theory were compared to numerical results obtained from ten computational constructs of monodisperse arrays of noninterpenetrating spheres (0.5 units in radius) randomly positioned in a three-dimensional space (20×20×20) with ε=0.80. The spheres were then numerically projected onto a two-dimensional surface for different values of D_f, and values of ε' and α' were computed.

Figure 1 shows a comparison between the numerical results from the sphere arrays and the predictions from the stereological theory with $D_p=(3\pi/2)(1-\varepsilon)/\alpha$. The agreement is excellent. Note that while ε' decreases uniformly as D_f increases, α' shows nonmonotonic behavior that increases with increasing D_f for $\alpha D_f/4\varepsilon<1$ and then decreases again toward zero for larger values of D_f.

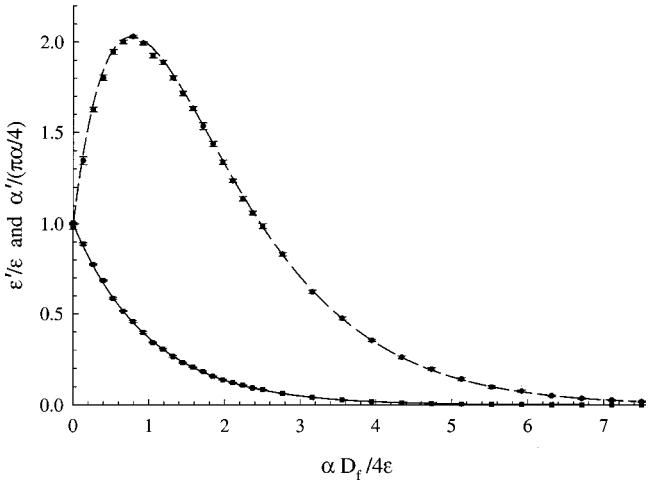

Fig. 1 ε' **and** $\alpha'/(\pi\alpha/4)$ **computed for randomly placed (noninterpenetrating) spheres that were numerically projected on a two-dimensional surface as a function of** $\alpha D_f/4\varepsilon$ **with** ε**=0.8. Squares are numerical results for** ε'**, circles for** $\alpha'/(\pi\alpha/4)$**. Error bars represent standard error. The solid line is prediction of equation (4***a***); the dashed line is prediction of equation (4***b***) with** $D_p=(3\pi/2)(1-\varepsilon)/\alpha$**.**

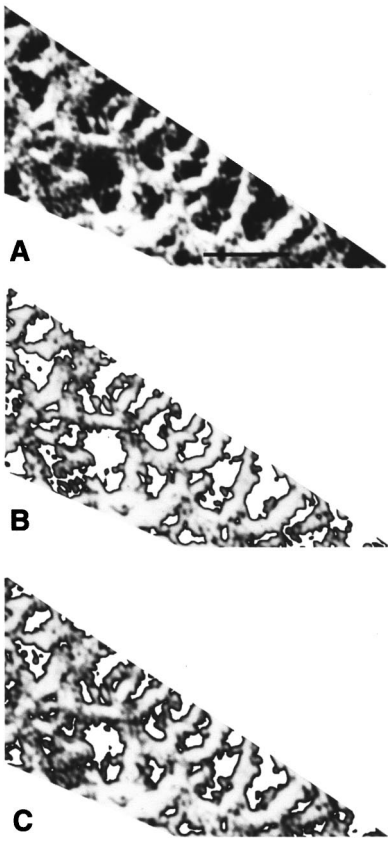

Fig. 3 (*a*) **Typical interfibrillar network chosen for specific hydraulic conductivity analysis;** (*b*) **high threshold image of open-spaces available for fluid flow that include 32.8 percent of the pixels (shown in white: pixel value >165: arbitrary units);** (*c*) **low threshold image of open-spaces available for fluid flow that include 17.8 percent of the pixels (pixel value >210). ×345,000; bar: 50 nm**

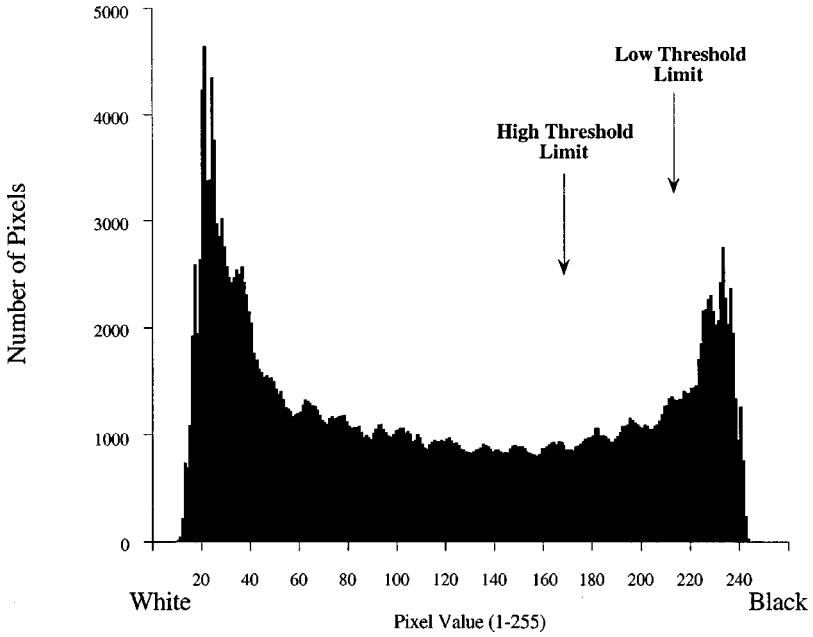

Fig. 4 Gray-scale histogram of the interfibrillar region shown in Fig. 3. Higher pixel values correspond to darker spaces. The high and low threshold limits are shown with the pixels on the right of each limit being defined as contributing to the open-spaces available for fluid flow.

3.2 Quick-Freeze/Deep-Etch Images of Corneal Stroma. Figure 2*a* shows a micrograph of the corneal stroma taken using conventional electron microscopy showing collagen fibers that are generally aligned in parallel arrays as would be expected in the corneal stroma. Figure 2*b* shows an image of the same tissue taken using quick-freeze/deep-etch; the enhanced resolution seen using quick-freeze/deep etch is stunning, demonstrating much greater ultrastructure in the interfibrillar matrix.

The three-dimensional appearance displays several interfibrillar structures which include unbranched, filamentous structures that are perpendicular to and appear to connect to adjacent collagen fibers (short arrows), while other branched filamentous structures form an interconnected network parallel to the collagen fibers (long arrows). In stereo pairs (not shown), these filamentous structures appear to connect to adjacent collagen fibers in different directions.

The diameter of the collagen fibers (23.6±0.5 nm; mean±S.E.) observed in the conventional TEM image are less than those values observed in the quick-freeze/deep-etch image (32.6±0.7 nm), consistent with the findings of other investigators that have used quick-freeze/deep-etch [26,27]. There is also an increased apparent density of collagen fibrils in Fig. 2*a* as compared with Fig. 2*b*. This is likely due to the greater depth-of-field of the conventional TEM image (90 nm, the section thickness), as compared to the quick-freeze/deep-etch image (15–51 nm: see below).

3.3 Morphometric Analysis of the Hydraulic Conductivity of Corneal Stroma. Figure 3*a* shows a typical interfibrillar region that was chosen for analysis. Figure 3*b* shows those pixels as white whose gray scale value is greater (i.e., darker) than the high threshold limit (large pores) for determining spaces that are available for fluid flow; Fig. 3*c* shows the analogous figure for the low threshold limit (small pores). Figure 4 illustrates the relative position of these threshold limits on a histogram of the pixel values determined from Fig. 3*a*. This histogram and relative position of threshold limits is representative of the other interfibrillar regions

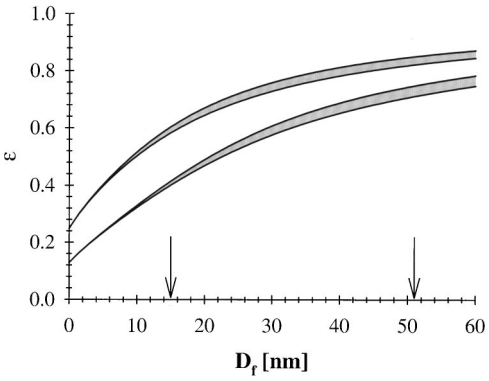

Fig. 5 Interfibrillar porosity (ε) of the hydrodynamically significant spaces as a function of depth-of-field (D_f). Two families of curves are shown, one for a low threshold level, the other high. For each threshold level, the shaded region represents the influence of particle shape [equation (5)]. The arrows indicate the minimum and maximum values of D_f.

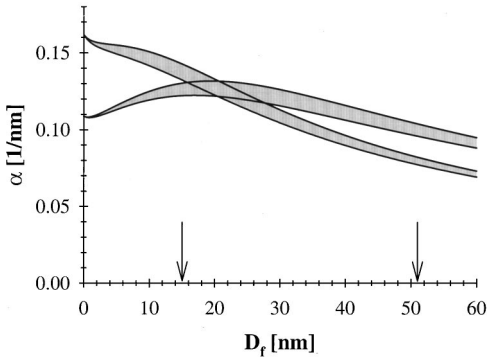

Fig. 6 Interfibrillar specific surface (α) of the hydrodynamically significant spaces as a function of depth-of-field (D_f). Labels as in Fig. 5.

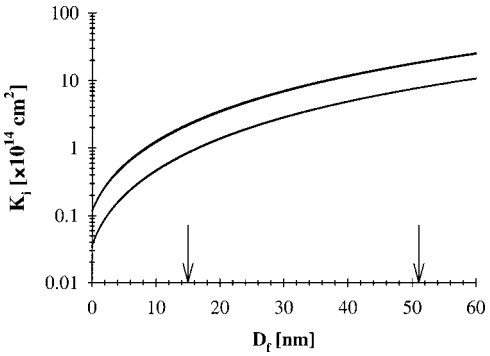

Fig. 7 Interfibrillar specific hydraulic conductivity (K_i) as a function of depth-of-field (D_f). Labels as in Fig. 5.

analyzed in this study. While these limits are admittedly somewhat subjective, they allow us to quantify the influence of pore size upon the specific hydraulic conductivity (K_i). For all values of D_f investigated, K_i never varied more than threefold between the minimum and maximum threshold limits.

Five micrographs were analyzed from three bovine corneas. To analyze variations of K_i within a single micrograph, ε' and α' were determined for each of five different interfibrillar regions within each micrograph. Averages were determined as the weighted-mean of these 25 measurements, with the weighting factor equal to the interfibrillar area of each region. To compute ε and α and thereby K_i, D_f was determined separately from three stereo images made from these same replicas. D_f was found to vary between 15 and 51 nm with a mean value of 28 ± 3 nm (mean$\pm$S.E., $n=15$). No relationship was seen between D_f and either ε' or α', but our data set was too small to reach any statistical conclusions.

The morphometric analysis yielded minimum threshold values of $\varepsilon'=0.128\pm0.015$ and $\alpha'=0.086\pm0.006$ nm^{-1} and maximum threshold values of $\varepsilon'=0.249\pm0.016$ and $\alpha'=0.127\pm0.005$ nm^{-1} (average$\pm$S.E.). Intramicrograph variability of ε' and α' between different interfibrillar regions average 26 and 19 percent, respectively. Using equations (4) and (5), ε and α were determined from the mean values of ε' and α' as a function of D_f, as shown in Figs. 5 and 6. Two families of curves are shown on each plot with each set of curves referring to a single level of thresholding. For each threshold level, two curves are shown, representing the influence of D_p, as it varies between a sphere and a cylinder [equation (5)]. In an analogous fashion, using equations (2), (4), and (5), K_i is predicted as a function of D_f, as shown in Fig. 7.

Using 15 nm$<D_f<$51 nm, and the range of curves seen in Fig. 7, K_i is found to vary between 0.84×10^{-14} cm^2 and 18.7×10^{-14} cm^2. Using equation (3), we find morphometrically determined specific hydraulic conductivity of the corneal stroma to vary between 0.46×10^{-14} cm^2 and 10.3×10^{-14} cm^2. These bounds include the range of values available in the experimental literature: 0.5×10^{-14} cm^2 and 2×10^{-14} cm^2 [9–13]. Furthermore, if we use the mean value for D_f of 28 nm, we find that the morphometrically determined specific hydraulic conductivity of the corneal stroma to vary between 1.4×10^{-14} and 3.6×10^{-14} cm^2, in very good agreement with experimentally measured values.

4 Discussion

While the hydraulic conductivities of a wide-variety of connective tissues have been measured experimentally [6], theories that predict the hydraulic conductivity of a connective tissue based upon either its composition or its morphological description have had, at best, limited success [5,6,28,29]. This discrepancy stems, at least in part, from the well-known difficulty of preserving the ultrastructure of glycosaminoglycans (GAGs) in conventional electron micrographs [7]. The highly charged GAGs, which maintain the structure of connective tissue [30], are bound to many extracellular moieties, and the collapse of the GAGs caused by heavy metal staining likely has significant effects on the ultrastructural appearance of the extracellular matrix.

We have demonstrated that morphometrically determined predictions of the specific hydraulic conductivity of a connective tissue, as seen by quick-freeze/deep etch, bound the experimentally measured values. Our predicted range of values spanned approximately one order of magnitude (0.46×10^{-14} cm^2 to 10.3×10^{-14} cm^2). This variability was due in large part to uncertainty in the determination of the depth-of-field of the replicas (see below). Use of the mean value for this parameter gave predictions for specific hydraulic conductivity (1.4×10^{-14} to 3.6×10^{-14} cm^2) that were in very good agreement with experimentally measured values (0.5×10^{-14} to 2×10^{-14} cm^2).

Our work using quick-freeze/deep-etch confirms that far better ultrastructural preservation of the corneal extracellular matrix is obtained using this technique as opposed to conventional electron microscopic techniques (Fig. 2). The excellent preservation of ultrastructural detail is most apparent in the interfibrillar matrix structure. We visualized filamentous structures that were perpendicular to and appear to connect adjacent collagen fibers, and other filamentous structures that form an interconnected network parallel to the collagen fibers. Similar observations have been made by other investigators using the quick-freeze/deep etch technique on corneal stroma [26,31]. However, we have not yet determined the identity of these structures. While these structures might be glycosaminoglycans, proteoglycans (biglycan, decorin or lumican), type VI collagen, or BIG H3 [32–35], identification of these structures will require use of immunogold methodology and/or enzymatic digestion studies.

Quick-freeze/deep-etch yields measurements of collagen fibril diameter that are similar to those obtained using freeze substitution and x-ray synchrotron examination, techniques developed to minimize preparation artifacts associated with standard transmission electron microscopy [36,19]. Glutaraldehyde fixation, used in this study for both conventional transmission electron microscopy and quick-freeze/deep-etch, induces a negligible change in the interfiber collagen spacing but leads to an increase in collagen fiber diameter of approximately 5 percent [37]. Subsequent dehydration and resin embedding during conventional processing decreases both collagen fiber diameter and interfiber spacing [19,37].

One potential caveat regarding these new structures that we have visualized is that we are viewing a replica of the tissue that involves the deposition of a platinum/carbon coating on an underlying substrate. One might make the analogy of examining bushes after a snowstorm. While the profile of the bush might be well-characterized by the snow, the finer structure of the leaves, individual branches and the spaces between them could be obscured by the surface coating. This same phenomenon occurs in our replicas.

The platinum-carbon layer coats the tissue with a layer that is approximately 1.5 nm thick (as controlled by a quartz crystal thin film monitor). This coating layer will decrease the apparent size of openings through which fluid can flow, and thereby decrease the apparent hydraulic conductivity of this tissue, as determined by morphometric analysis. The effect of this layer on the calculated value of K can be estimated by considering the average hydraulic diameter of the corneal stroma, which can be estimated as typically done in porous media as $4\varepsilon/\alpha$. Using $\varepsilon=0.6$ and $\alpha=0.13$ nm^{-1} (see Figs. 5 and 6), we find a hydraulic diameter of 18 nm. While the coating thickness is non-negligible, it can be seen that it will not affect the order-of-magnitude of our estimate; however, it does suggest that our calculated value of K is likely to be a lower bound.

We found a porosity of the open-space (ε) of between 55 and 75 percent (mean value of D_f: see Fig. 4). However, the cornea is

known to have a water content of approximately 80 percent and the interfibrillar space has a water content higher than this [19]. This would lead to the conclusion that while the open-spaces we viewed are genuine, there are likely many small open-spaces within the intefibrillar matrix that are not visualized due to the coating layer.

Indeed, our predictions of interfibrillar space available for fluid flow ($\varepsilon=0.4-0.8$) are much smaller than would be expected based on the reported interfibrillar volume fractions of extracollagenous material ($\phi_{GAG}=9.5\times10^{-3}$ and $\phi_{PG}=2.43\times10^{-2}$) which would lead one to anticipate a value of ε of roughly 0.975 [15,5,6]. Part of this difference would likely result from the presence of type VI collagen, which is known to exist in the bovine corneal stroma [38] and has been shown to be present in high concentrations (17 to 25 percent of corneal dry weight [34]) within the interfibrillar space of the human corneal stroma [39]. Furthermore, there is certainly a significant reduction in open-space due to the coating layer that preferentially obscures the smaller intramolecular and intermolecular spaces. Due to the smaller hydrodynamic diameter of these openings, however, flow through these pathways would presumably be negligible compared to the flow through the more hydrodynamically significant pores that we have identified. With flow confined to the larger pores observed on the replicas, we are justified in the use of a Kozeny constant of 5 appropriate for a low porosity ($\varepsilon<0.8$) porous medium [17].

The success of our model in bounding the available experimental data is encouraging and suggests that we may indeed be visualizing the ultrastructural components of the extracellular matrix responsible for generating the flow resistance of the corneal stroma. However, there are several other assumptions made in our hydrodynamic analysis that must be recognized. These include the determination of the depth-of-field of the replicas, the role of thresholding in defining the hydraulically significant spaces and the assumption of a homogenous pore size in the porous medium necessary to allow use of Carmen-Kozeny theory.

The depth-of-field has the largest effect upon our estimate of hydraulic permeability, yielding order-of-magnitude changes in the range of D_f investigated. The depth to which the platinum-carbon mixture penetrates the etched tissue may vary between interfibrillar regions due to differences in evaporation rate and inhomogeneities in tissue structure. No one value of D_f could be used to describe each of the 25 interfibrillar regions analyzed in this study. We thus attempted to determine a range of D_f that would include an appropriate depth-of-field for each region. This range was determined from the maximum and minimum values of D_f measured from the deepest observed structures in three of the corneal stereo micrographs included in this study. This range thus represents our most conservative estimate of D_f that contributes to our predicted range of hydraulic permeability.

Thresholding necessarily introduced a subjective element into our characterization of the hydrodynamically significant spaces. These threshold limits were carefully chosen to bound the range of visually acceptable pore size. The high threshold limit (Fig. 3*b*) was defined as the pixel value where the pore perimeter began to encroach upon the interfibrillar structure. Increasing the threshold beyond this limit would incorporate into these pores those pixels that are visually interpreted to be part of the matrix structure. The low threshold limit (Fig. 3*c*) was chosen to represent the minimum acceptable pore size, where further reductions in threshold would result in an inordinate erosion of pore perimeter leading to disjoint pore subunits. The threshold limits thus represent our most conservative estimates of the upper and lower bounds of pore size. We demonstrated that when comparing the lowest reasonable threshold value to the highest, we saw a change of approximately a factor of 2.5, which is substantially less than the changes observed by the determined range of depth-of-field. Thus, while it would be desirable to define more quantitative estimates of pore size, the subjective aspects of the analysis do not fundamentally affect our conclusions.

Carmen-Kozeny theory implicitly assumes that a single pore size characterizes the porous medium. This can be seen by examining equation (2): if a medium is composed of two pores sizes, one large, the other very small, then the only contribution of the small pores will be to increase α, and thus decrease K. However, the Kelvin minimum energy theorem can be used to show that adding pores to a porous medium cannot, for conditions of viscous flow, decrease K [40]. As the magnification of an image is increased, the fractal nature of most objects leads to the addition of tiny pores to the morphological description of a medium that Carmen-Kozney theory would necessarily have to exclude. We considered this phenomenon by varying the size of the minimum pore diameter we included in our hydrodynamic analysis and found that this phenomenon is not significant in a homogeneous structure such as the corneal stroma (data not shown).

Our studies have demonstrated that the quick-freeze/deep-etch technique can visualize ultrastructural elements of the extracellular matrix of the corneal stroma that are not seen using conventional techniques, and these structures may responsible for generating the high flow resistance characteristic of connective tissues. We have further demonstrated that when examining connective tissues at these high levels of resolution, quantitative analyses require advanced stereological corrections to be employed to correct for a variety of artifacts, most notably the depth-of-field of the image.

It is appropriate to end by commenting on the physiological relevance of corneal hydraulic conductivity. While flow through corneal stroma under normal conditions has been observed [41,42], this flow has not been shown to have physiological importance. However, flow through other connective tissue matrices such as cartilage [43], renal glomerulus [3], and the aqueous outflow system in the eye [44] have high physiological significance. Corneal stroma is a useful model system for studying extracellular matrix hydraulic conductivity using this morphometric technique because it is a very well characterized tissue whose hydraulic conductivity [9–13] and biochemical composition [45] are well-known. By demonstrating that the morphological ultrastructure of the extracellular matrix of corneal stroma is consistent with its measured hydraulic conductivity, we have demonstrated that these structures may indeed be responsible for generating tissue flow resistance. This is the first time, to our knowledge, that such a correspondence has been made for a connective tissue, and analogous studies will hopefully demonstrate whether a similar relationship can be found in other connective tissues.

The specific hydraulic conductivity of corneal stroma can be experimentally measured without utilizing the morphometric methods described here [9,12]. However, there are a number of tissues in the body that are important regulators of fluid transport that are difficult to isolate so that direct measurements of hydraulic conductivity may be made. Examples of such tissues include the juxtacanalicular connective tissue of the eye (as related to glaucoma) [5], Bruch's membrane (as related to age-related macular degeneration) [46], the basement membrane surrounding retinal blood vessels (diabetes) [47], and the glomerular basement membrane (kidney diseases) [48]. While biochemical analysis provides a powerful method for making indirect determinations of specific hydraulic conductivity [6], it necessarily assumes a homogenous extracellular matrix; and in some tissues (e.g., juxtacanalicular connective tissue) this method does not have sufficient spatial resolution to determine the specific matrix components that are responsible for generating the flow resistance. Morphometric methods add a powerful tool that in conjunction with biochemical methods will allow characterization of specific hydraulic conductivity beyond the limitations of direct hydrodynamic methods. Combining this morphometric technique with immunolocalization

studies could potentially identify pathologic alterations in extracellular matrix ultrastructure that are responsible for disrupting transport in connective tissues.

Appendix

To estimate the specific hydraulic conductivity of the corneal stroma using Carmen-Kozeny theory, we require ε and α, parameters that characterize the geometry of the three-dimensional porous medium through which fluid flows. However, the micrographs that we use to examine the structure of the open-spaces in the corneal stroma allow us only to compute the two-dimensional parameters ε' and α', the result of a projection of the three-dimensional structure onto a two-dimensional image. We here describe how these two parameters are used, in conjunction with estimates of D_f, generated from stereo image pairs, to estimate ε and α. We follow, in general, the methodology of Underwood [23] and Miles [22], although we explicitly account for the volume exclusivity of the particles. We here just give a brief summary of the steps.

Consider a volume V of a medium that is comprised of particles *randomly* placed and oriented, without interpenetrating, in a three-dimensional space. Let $V=A^*D_f$ where A is the area of the micrograph. Then the total volume of solids in this medium is $(1-\varepsilon)^*A^*D_f$ and the wetted surface area is $\alpha^*A^*D_f$.

As D_f increases, ε' decreases since the surface area of more of the particles are projected onto the micrograph. We consider a plane parallel to the micrograph at a distance D_f away and let n be the number of particles per unit area that pass through this plane. If we let A_p be the average projected area of one of the particles onto a 2D surface, then,

$$\frac{d\varepsilon'}{dD_f} = -\frac{1}{A}\sum_{j=1}^{n}\left(\frac{dA_p}{dD_f}\right)_j (P_{\mathrm{no}})_j \tag{A1}$$

where P_{no} is the probability that projection of the jth particle intersecting the plane at D_f does not overlap with any particle already projected.

The probability P_{no} can be computed as the ratio of (i) the available space for placement of dA_p that does not overlap with the projection of any particle already projected to (ii) the total area available for placement of dA_p that does not intersect any other particle at D_f. The former quantity is $\varepsilon' A$, while the latter is εA, yielding $P_{\mathrm{no}}=\varepsilon'/\varepsilon$.

We here introduce two probability density functions for the particle centroid location (f_V) and the particle orientation (f_Ω) that allow us to convert the sum in equation (*A*1) to an integral:

$$\frac{d\varepsilon'}{dD_f} = -\frac{\varepsilon'}{A\varepsilon}\int_V\int_\Omega \frac{dA_p}{dD_f} f_{\mathbf{V}} f_{\mathbf{\Omega}} d\mathbf{\Omega} d\mathbf{V} \tag{A2}$$

where $\int f_{\mathbf{V}} d\mathbf{V} = \mathrm{NV}$, N is the number of particles per unit volume, Ω is the solid angle (or orientation) of the particle, and $\int f_\Omega d\Omega = 1$. Equation (*A*2) can also be expressed as

$$\frac{d\varepsilon'}{dD_f} = -\frac{\varepsilon'}{A\varepsilon}\frac{d}{dD_f}\int_V\int_\Omega A_p f_{\mathbf{V}} f_{\mathbf{\Omega}} d\mathbf{\Omega} d\mathbf{V} \tag{A3}$$

The projected area of a convex particle with random orientation can be related to the surface area (S) of that particle by integrating over all orientations. This yields the Cauchy relationship [49,50]

$$S = 4\int_\Omega A_p(\mathbf{\Omega}) f_{\mathbf{\Omega}} d\mathbf{\Omega} \tag{A4}$$

Recognizing that, for volume excluding particles, the surface area of a particle is related to α as: $\alpha=\mathrm{NS}$, we use equations (*A*3) and (*A*4) to find that

$$\frac{d\varepsilon'}{dD_f} = -\frac{\varepsilon'\alpha}{4\varepsilon} \tag{A5}$$

We now seek a second differential equation that describes how α' changes with increasing D_f. This is more complicated than the case of ε', since increasing D_f can either increase or decrease α' depending on the values of ε' and α'. Analogous to equation (*A*1), increasing D_f will increase the projected perimeter of those particles that pass through the plane at a distance D_f from the projected plane. However, the increased projected area of these particles may also overlap the border of those particles that already are projected, leading to a reduction in α' that is proportional to the increased projected area (dA_p) and to the already projected perimeter ($\hat{\alpha}' A$) that overlaps the spaces available for particle placement (εA). Letting P_p be the average projected perimeter of a particle, we find that:

$$\frac{d\alpha'}{dD_f} = \frac{1}{A}\sum_{j=1}^{n}\left[\left(\frac{dP_p}{dD_f}\right)_j (P_{\mathrm{no}})_j - \left(\frac{dA_p}{dD_f}\right)_j \frac{\hat{\alpha}'}{\varepsilon}\right] \tag{A6}$$

$\hat{\alpha}'$ is only a fraction of the total projected perimeter, α', since the increment in projected area of a particle (dA_p) cannot overlap itself nor can it overlap other particles in its same plane at D_f (due to volume exclusivity). Thus, $\hat{\alpha}' = \alpha' - \alpha'_T$ where α'_T is the projected perimeter of those particles truncated by the plane at D_f.

The expected projected perimeter of any isolated particle intersecting a plane can be found as $\alpha'_j = (\pi/4)\alpha_j$ [25]. The projected perimeter $\alpha_T = \Sigma\alpha'_j$ of all of the truncated particles at D_f is reduced due to overlap with the particles below that plane such that $\alpha'_T = P_{\mathrm{no}}\alpha_T$. We thus find that

$$\frac{d\alpha'}{dD_f} = \frac{1}{A}\sum_{j=1}^{n}\left[\left(\frac{dP_p}{dD_f}\right)_j (P_{\mathrm{no}})_j - \left(\frac{dA_p}{dD_f}\right)_j \frac{\alpha'}{\varepsilon} + \left(\frac{dA_p}{dD_f}\right)_j \varepsilon' \frac{\alpha\pi}{4\varepsilon^2}\right] \tag{A7}$$

Then, defining $D_p \equiv \pi A_p / P_p$, and following the same procedure used to derive equation (*A*5), equation (*A*7) becomes

$$\frac{d\alpha'}{dD_f} = \frac{\alpha}{4\varepsilon}\left[\frac{\pi}{D_p}\varepsilon' - \alpha' + \varepsilon'\frac{\alpha\pi}{4\varepsilon}\right] \tag{A8}$$

We apply the conditions that $\varepsilon'(D_f=0)=\varepsilon$ and $\alpha'(D_f=0)=(\pi/4)\alpha$ [25]. Solving equations (*A*5) and (*A*8) with these conditions yields equations (4*a*) and (4*b*). The equations are similar to those derived by Miles [22] who formulated this problem allowing particles to overlap. If we relax the restrictions on volume exclusivity, then Miles' results are recovered.

Equations (*A*5) and (*A*8) are different from the relationships derived by Underwood [23] whose results did not satisfy the boundary conditions given here. Underwood also did not consider the volume exclusivity of the particles.

At this point, equation set (4*a*) and (4*b*) still involves an undetermined parameter, namely, D_p. However, by assuming that the particles are convex, we can put tight constraints on its value. In particular, for spherical particles, $D_p=(3\pi/2)(1-\varepsilon)/\alpha$ whereas for cylindrical particles, $D_p=(2\pi)(1-\varepsilon)/\alpha$. Assuming the particle shape to be between these two limits, the value of D_p can be constrained as shown in equation (5).

Acknowledgments

We acknowledge support from the Whitaker Foundation, the National Eye Institute, EY09699, and unrestricted departmental grants from Research to Prevent Blindness, Inc., The Massachusetts Lions Eye Research Fund, Inc., to Boston University. We also acknowledge use of NIH Image version 1.62, and thank Dr. Yuan Chen for use of his image flipper code.

References

[1] Knight, A. D., and Levick, J. R., 1985, ''Effect of Fluid Pressure on the Hydraulic Conductance of Interstitium and Fenestrated Endothelium in the Rabbit Knee,'' J. Physiol. (London), **360**, pp. 311–332.

[2] Urban, J. P. G., and Maroudas, A., 1980, ''The Chemistry of the Intervertebral

in Relation to its Physiological Function and Requirements,'' Clin. Rheum. Dis., **6**, pp. 51–76.
[3] Daniels, B. S., Hauser, E. B., Deen, W. N., and Hostetter, T. H., 1992, ''Glomerular Basement Membrane: in Vitro Studies of Water and Protein Permeability,'' Am. J. Physiol., **262**, pp. F919–F926.
[4] Bito, L. Z., Davson, H., and Fenstermacher, J. D., 1977, *The Ocular and Cerebrospinal Fluids*, Academic Press, London, New York, San Francisco.
[5] Ethier, C. R., Kamm, R. D., Palaszewski, B. A., Johnson, M. C., and Richardson, T. M., 1986, ''Calculations of Flow Resistance in the Juxtacanalicular Meshwork,'' Invest. Ophthalmol. Visual Sci., **27**, pp. 1741–1750.
[6] Levick, J. R., 1987, ''Flow Through Interstitium and Other Fibrous Matrices,'' Q. J. Exp. Physiol., **72**, pp. 409–437.
[7] Hascall, V. C., and Hascall, G. K., 1982, ''Proteoglycans,'' *Cell Biology of Extracellular Matrix*, E. D. Hay, ed., Plenum Press, New York, pp. 39–63.
[8] Mecham, R. P., and Heuser, J., 1990, ''Three-Dimensional Organization of Extracellular Matrix in Elastic Cartilage as Viewed by Quick Freeze, Deep Etch Electron Microscopy,'' Connect. Tissue Res., **24**, pp. 83–93.
[9] Hedbys, B. O., and Mishima, S., 1962, ''Flow of Water in Corneal Stroma,'' Exp. Eye Res., **1**, pp. 262–275.
[10] Hedbys, B. O., 1963, ''Corneal Resistance to the Flow of Water After Enzymatic Digestion,'' Exp. Eye Res., **2**, pp. 112–121.
[11] Hedbys, B. O., and Mishima, S., 1969, ''The Flow of Water Across the Corneal Layers,'' *The Cornea, Macromolecular Organization of a Connective Tissue*, M. Langham, ed., Johns Hopkins, Baltimore, pp. 69–77.
[12] Fatt, I., and Hedbys, B. O., 1970, ''Flow Conductivity of Human Corneal Stoma,'' Exp. Eye Res., **10**, pp. 237–242.
[13] Eisenberg, S. R., and Grodzinsky, A. J., 1987, ''The Kinetics of Chemically Induced Nonequilibrium Swelling of Articular Cartilage and Corneal Stroma,'' J. Biomech. Eng., **109**, pp. 79–89.
[14] Carmen, P. C., 1937, ''Fluid Flow Through Granular Beds,'' Trans. Inst. Chem. Eng., **15**, pp. 150–166.
[15] Ethier, C. R., 1983, ''Hydrodynamics of Flow Through Gels With Applications to the Eye,'' *Mechanical Engineering*, Massachusetts Institute of Technology, Cambridge, MA.
[16] Bird, R. B., Stewart, W. E., and Lightfoot, E. N., 1960, *Transport Phenomena*, Wiley, New York.
[17] Happel, J., and Brenner, H., 1983, *Low Reynolds Number Hydrodynamics*, Martinus Nijhoff, Hague, Netherlands.
[18] Ghaddar, C. K., 1995, ''On the Permeability of Unidirectional Fibrous Media: A Parallel Computational Approach,'' Phys. Fluids, **7**, pp. 2563–2586.
[19] Meek, K., Fullwood, N., Cooke, P., Elliot, G., Maurice, D., Quantock, A., Wall, R., and Worthington, C., 1991, ''Synchrotron X-Ray Diffraction Studies of the Cornea, With Implications for Stromal Hydration,'' Biophys. J., **60**, pp. 467–474.
[20] Ethier, C. R., 1991, ''Flow Through Mixed Fibrous Porous Materials,'' AIChE J., **37**, pp. 1227–1236.
[21] Paleszewski, B., 1983, *Analytical Studies of Flow Through a Porous Medium With Applications to the Trabecular Meshwork of the Eye*, Massachusetts Institute of Technology, Cambridge, MA.
[22] Miles, R. E., 1975, ''On Estimating Aggregate and Overall Characteristics From Thick Sections by Transmission Electron Microscopy,'' *Proceedings of the Fourth International Congress for Stereology*, National Bureau of Standards Special Publications, Gaithersburg, MD.
[23] Underwood, E. E., 1970, *Quantitative Stereology*, Addison-Wesley, Reading, MA.
[24] Delesse, A., 1848, ''Pour Determiner la Composition des Roches,'' Ann. Mines, **13**, pp. 379–388.
[25] Saltykov, S. A., 1958, *Stereometric Metallography*, Metallurgizdat, Moscow.
[26] Hirsch, M., Nicholas, G., and Pouliquen, Y., 1989, ''Interfibrillar Structures in Fast-Frozen, Deep-Etched and Rotary-Shadowed Extracellular Matrix of Rabbit Corneal Stroma,'' Exp. Eye Res., **49**, pp. 311–315.
[27] Yamabayashi, S., Ohno, S., Aguilar, R. N., Furuya, T., Hosoda, M., and Tsukahara, S., 1991, ''Ultrastructural Studies of Collagen Fibers of the Cornea and Sclera by a Quick-Freezing and Deep-Etching Method,'' Ophthalmic Res., **23**, pp. 320–329.
[28] Huang, Y., Rumschitzki, D., Chien, S., and Weinbaum, S., 1994, ''A Fiber Matrix Model for the Growth of Macromolecular Leakage Spots in the Arterial Intima,'' J. Biomech. Eng., **116**, pp. 430–445.
[29] Huang, Y., Rumschitzki, D., Chien, S., and Weinbaum, S., 1997, ''A Fiber Matrix Model for the Filtration Through Fenestral Pores in a Compressible Arterial Intima,'' Am. J. Physiol., **272**, pp. H2023–H2039.
[30] Comper, W. D., and Laurent, T. C., 1978, ''Physiological Function of Connective Tissue Polysaccharides,'' Physiol. Rev., **58**, pp. 255–315.
[31] Hirsch, M., Noske, W., Prenant, G., and Renard, G., 1999, ''Fine Structure of the Developing Avian Corneal Stroma as Revealed by Quick-Freeze/Deep-Etch Electron Microscopy,'' Exp. Eye Res., **69**, pp. 267–277.
[32] Anseth, A., and Laurent, T., 1961, ''Studies on Corneal Polysaccharides. I. Separation.,'' Exp. Eye Res., **1**, pp. 25–38.
[33] Axelsson, I., and Heinegard, D., 1975, ''Fractionation of Proteoglycans From Bovine Corneal Stroma,'' Biochem. J., **145**, pp. 491–500.
[34] Zimmermann, D., Trueb, B., Winterhalter, K., Witmer, R., and Fischer, R., 1986, ''Type VI Collagen Is a Major Component of the Human Cornea,'' FEBS Lett., **197**, pp. 55–58.
[35] Rawe, I., Zhan, Q., Burrows, R., Bennet, K., and Cintron, C., 1997, ''Beta-ig. Molecular Cloning and In Situ Hybridization in Corneal Tissues,'' Invest. Ophthalmol. Visual Sci., **38**, pp. 893–901.
[36] Craig, A., Robertson, J., and Parry, D., 1986, ''Preservation of Corneal Collagen Fibril Structure Using Low-Temperature Procedures for Electron Mmicroscopy,'' J. Ultrastruct Mol. Struct. Res., **96**, pp. 172–175.
[37] Fullwood, N., and Meek, K., 1993, ''A Synchroton X-Ray Study of the Changes Occurring in the Corneal Stroma During Processing for Electron Microscopy,'' J. Microsc., **169**, pp. 53–60.
[38] Murata, Y., Yoshioka, H., Iyama, K., and Usuku, G., 1989, ''Distribution of Type VI Collagen in the Bovine Cornea,'' Ophthalmic Res., **21**, pp. 67–72.
[39] Marshall, G. E., A. G., K., and W.R., L., 1991, ''Immunogold Fine Structural Localization of Extracellular Matrix Components in Aged Human Cornea. II. Collagen Types V and VI,'' Graefe's Arch. Clin. Exp. Ophthalmol., **229**, pp. 164–171.
[40] Hill, R., and Power, G., 1956, ''Extremum Principles for Slow Viscous Flow and the Approximate Calculation of Drag,'' Q. J. Mech. Appl. Math., **9**, pp. 310–319.
[41] Mishima, S., and Maurice, D., 1961, ''The Oily Layer of the Tear Film and Evaporation From the Corneal Surface,'' Exp. Eye Res., **1**, pp. 39–45.
[42] Wiig, H., 1990, ''Cornea Fluid Dynamics II. Evidence for Transport of Radiolabelled Albumin in Rabbits by Bulk Flow,'' Exp. Eye Res., **50**, pp. 261–267.
[43] Mow, V. C., Holmes, M. H., and Lai, W. M., 1984, ''Fluid Transport and Mechanical Properties of Articular Cartilage: A Review,'' J. Biomech., **17**, p. 377.
[44] Bill, A., 1984, ''Circulation in the Eye,'' *Microcirculation, Part 2*, E. M. Renkin and C. C. Michel, eds., American Physiological Society, Baltimore, MD, IV, p. 1076.
[45] Fatt, I., 1978, *Physiology of the Eye: An Introduction to the Vegetative Functions*, Butterworth, Boston, MA.
[46] Starita, C., Hussain, A., Pagliarini, S., and Marshall, J., 1996, ''Hydrodynamics of Aging Bruch's Membrane: Implications for Macular Disease,'' Exp. Eye Res., **62**, pp. 565–572.
[47] Robinson, W., Kador, P., and Kinoshita, J., 1983, ''Retinal Capillaries: Basement Membrane Thickening by Galactosemia Prevented With Aldose Reductase Inhibitor,'' Science, **221**, pp. 1177–1179.
[48] Drumond, M., and Deen, W., 1994, ''Stokes Flow Through a Row of Cylinders Between Parallel Walls: Model for the Flomerular Slit Diaphragm,'' J. Biomech. Eng., **116**, pp. 184–189.
[49] Cauchy, A., 1908, *Oeuvres Completes d'Augustin Cauchy*, Gauthier-Villars, Paris.
[50] Vouk, V., 1948, ''Projected Area of Convex Bodies,'' Nature (London), **162**, p. 330.